Noname manuscript No.
(will be inserted by the editor)

Corrections for one- and two-point statistics measured with coarse-resolution Particle Image Velocimetry

Antonio Segalini · Gabriele Bellani · Gaetano Sardina · Luca Brandt · Evan A. Variano

Received: date / Accepted: date

Abstract A theoretical model to determine the effect of the size of the interrogation window in Particle Image Velocimetry measurements of turbulent flows is presented. The error introduced by the window size in two-point velocity statistics, including velocity autocovariance and structure functions, is derived for flows that are homogeneous within a 2D plane or 3D volume. This error model is more general than those previously discussed in the literature, and provides a more direct method of correcting biases in experimental data. Within this model framework, simple polynomial approximations are proposed to provide a quick estimation of the effect of the averaging on these statistics. The error model and its polynomial approximation are validated using statistics of homogeneous isotropic turbulence obtained in a physical experiment and in a direct numerical simulation. The results demonstrate that the present formulation is able to correctly estimate the turbulence statistics, even in the case of strong smoothing due to a large interrogation window. We discuss how to use these results to correct experimental data and to aid the comparison of numerical results with laboratory data.

Keywords Isotropic turbulence · PIV · Spatial resolution

1 Introduction

Particle Image Velocimetry (PIV) is a measurement technique that allows the characterization of a velocity field in space and time by calculating the displacement of groups of tracer particles in "interrogation areas", which are discrete sub-regions of the measurement area (Raffel et al, 2001; Adrian, 2005). From a theoretical point of view, the PIV algorithm can be seen as a spatio-temporal filter (see Westerweel, 1997) of the velocity field, whose cut-off frequency and wavelength depends mainly

A. Segalini, G. Sardina, L. Brandt,
Linné FLOW Centre, KTH Mechanics
100-44 Stockholm, Sweden E-mail: segalini@mech.kth.se

G. Bellani, E. A. Variano,
Department of Civil and Environmental Engineering
University of California, Berkeley, CA 94720, USA

on the interval between two subsequent images, Δt, and the size of the interrogation area, L, respectively. The first can be made very small thanks to double-cavity lasers, which can shoot two pulses at arbitrarily small intervals, and efficient subpixel interpolation schemes that can precisely resolve small displacements caused by small Δt values (Chen and Katz, 2005; Nobach et al, 2005). The frequency resolution is also increasing due to improved cameras and algorithms (see Scarano and Moore, 2012). Spatial resolution of PIV has also been improved by new algorithms, e.g. those with iterative window offset and deformation (Westerweel et al, 1997; Scarano and Riethmuller, 2000; Scarano, 2002). However, PIV spatial resolution is always limited by the fundamental trade-off between interrogation area size and signal strength. That is, reducing the size of the interrogation area reduces the number of tracer particles used in the velocity calculation, having a negative effect on the signal-to-noise ratio (see Westerweel, 1997; Foucaut et al, 2004). This constraint leads to a minimum size of the interrogation area, given the practical limits of tracer particle density (Kähler et al, 2012; Poelma et al, 2006) and limits the spatial resolution capability of PIV. According to the latest comparative tests, it is very difficult in practice to use an interrogation window smaller than 16×16 pixels (Stanislas et al, 2008). In physical space, this corresponds to a window size that ranges between 0.5×0.5 mm^2 and 2×2 mm^2 for common optical setups (*e.g.*, camera resolution 1024×1024 pixels and 50×50 mm^2 or 100×100 mm^2-wide image areas). These values can be significantly higher than the smallest turbulent scales at high-Reynolds number, thus the effect of the unresolved scales must be taken into account.

Typical PIV data analyses use the velocity fields to compute quantities such as the spatial distribution of turbulent kinetic energy (TKE), vorticity, dissipation rate and two-point correlations. It is well known that the estimation of such quantities is strongly affected by spatial resolution (Saarenrinne et al, 2001). *Ad hoc* correction schemes can account for insufficient resolution for some specific quantities, such as the velocity variance (Saarenrinne and Piirto, 2000; Tanaka and Eaton, 2007; Scharnowski et al, 2012).

One-dimensional filtering effects can occur in more traditional measurement techniques, for instance in hot-wire anemometry, due to the finite length of the sensor. This problem was first addressed by Dryden et al (1937) and further investigated by Frenkiel (1949), Wyngaard (1968) and Segalini et al (2011a) among others, which proposed several correction schemes for hot-wire measurements. In particular Wyngaard (1968) provided an elegant analysis in Fourier space of the effect of spatial resolution in single- or X-wire measurements in isotropic turbulence.

Several papers address spatial resolution issues for PIV (see for example Scarano, 2003; Lavoie et al, 2007; Giordano and Astarita, 2009; Kähler et al, 2012). In particular, Lavoie et al (2007) extended the methodology of Wyngaard (1968) to estimate 2D filtering effects in PIV data of grid turbulence, assuming a flow field that is statistically homogeneous and isotropic.

In this paper, similarly to the work of Lavoie et al (2007), we derive a rigorous analytical model of the 2D-filtering effects for flows that are homogeneous within a 2D plane, but we do so in physical space, rather than in wavenumber space. The advantage of this approach is that it relates filtering effects to physical quantities like the Taylor length scale, and it is easily implemented in experimental data. Furthermore, the assumptions of homogeneity and isotropy are slightly relaxed, as only planar homogeneity is required for a general correction. The analytical model is validated against well-resolved experimental and numerical velocity fields of Homogeneous Isotropic Turbulence (HIT), which are then filtered with increasingly larger averaging windows to simulate the effect of a coarser PIV grid. The variation of statistical quantities (variance, correlation curves, and structure functions) with resolution is then compared to the prediction of the theoretical model.

The paper is structured as follows: The theoretical model is described in section 2. Sections 3 and 4 report the details of the numerical simulations and of the laboratory experiment, respectively, while section 5 shows the comparison of the proposed theory with the data. Finally, some discussions regarding the proposed methodology and its application in the experimental practice (including the numerical-experimental comparison) are presented in section 6.

2 Analytical model

As justified in the appendix, we begin with the simple postulate that the measured (or filtered) velocity, $\boldsymbol{V}_m$, is given by the spatial average of the velocity field over a planar domain D of size $L \times L$ together with some small measurement noise

$$\boldsymbol{V}_m\left(\boldsymbol{X_0}\right) = \frac{1}{L^2}\int_D \boldsymbol{V}\left(\boldsymbol{x},t\right)\mathrm{d}\boldsymbol{x} + \boldsymbol{\epsilon}\left(\boldsymbol{X_0}\right), \tag{1}$$

where $\boldsymbol{X_0}$ is the center of D, $\boldsymbol{V}\left(\boldsymbol{x},t\right) : \{v_1, v_2, v_3\}$ is the unfiltered velocity field, $\boldsymbol{x} : \{x_1, x_2\}$ is the planar domain (in which D lies), and t is time. The first consequence of equation (1) is that the measured mean velocity is also given by the integral average of the mean velocity field, namely

$$\langle \boldsymbol{V} \rangle_m \left(\boldsymbol{X_0}\right) = \frac{1}{L^2}\int_D \langle \boldsymbol{V}\left(\boldsymbol{x},t\right)\rangle \mathrm{d}\boldsymbol{x} + \langle \boldsymbol{\epsilon}\left(\boldsymbol{X_0}\right)\rangle, \tag{2}$$

where the brackets $\langle\cdot\rangle$ indicate the time average operator. If the field is homogeneous, or varying on a length scale much larger than L, the spatial resolution has no effect on the measured mean velocity, but the averaged noise might have some effects. However, here and in the followings it will be assumed that the measurement-noise in the i^{th} velocity component, $\epsilon_i\left(\boldsymbol{X_0}\right)$, is white noise, namely that it is uncorrelated in space and time with mean $\langle \epsilon_i\left(\boldsymbol{X_0}\right)\rangle = 0$ and variance $\langle \epsilon_i^2\left(\boldsymbol{X_0}\right)\rangle = \sigma_\epsilon^2$, independently of the position $\boldsymbol{X_0}$ and velocity component. Furthermore, it will be assumed that the measurement noise is uncorrelated with the instantaneous velocity field.

By introducing the Reynolds decomposition, $\boldsymbol{v} = \boldsymbol{V} - \langle \boldsymbol{V}\rangle$, we can now express the measured covariance matrix (Reynolds stresses) as

$$\langle v_i v_j \rangle_m \left(\boldsymbol{X_0}\right) = \frac{1}{L^4}\int_D\int_D \langle v_i\left(\boldsymbol{x},t\right) v_j\left(\boldsymbol{x'},t\right)\rangle \mathrm{d}\boldsymbol{x}\mathrm{d}\boldsymbol{x'} + \langle \epsilon_i\left(\boldsymbol{X_0}\right)\epsilon_j\left(\boldsymbol{X_0}\right)\rangle. \tag{3}$$

Unlike mean quantities, the measured value of the covariance (as well as the statistical moments of higher order) is attenuated by the spatial filtering even when the flow is statistically homogeneous, while the effect of the measurement noise is important only for the velocity variances, since the cross correlation

$\langle \epsilon_i(\boldsymbol{X_0})\,\epsilon_j(\boldsymbol{X_0})\rangle = 0$ if $i \neq j$ by hypothesis. We will now compute this attenuation as a function of the window size and of a characteristic length scale of the flow.

Consider the measured two-point velocity correlation

$$\langle v_i(\boldsymbol{a})\,v_j(\boldsymbol{b})\rangle_m = \frac{1}{L^4}\int_{D_a}\int_{D_b}\langle v_i(\boldsymbol{a}+\boldsymbol{x},t)\,v_j(\boldsymbol{b}+\boldsymbol{x'},t)\rangle\,\mathrm{d}\boldsymbol{x}\mathrm{d}\boldsymbol{x'} + \langle \epsilon_i(\boldsymbol{a})\,\epsilon_j(\boldsymbol{b})\rangle\,, \tag{4}$$

where D_a and D_b indicate the interrogation windows centered in the points $\boldsymbol{a}$ and $\boldsymbol{b}$, respectively. If we define the unfiltered two-point correlation tensor R_{ij} as

$$R_{ij}(\boldsymbol{p},\boldsymbol{q}) = \frac{\langle v_i(\boldsymbol{p},t)\,v_j(\boldsymbol{q},t)\rangle}{\left[\langle v_i^2(\boldsymbol{0})\rangle\langle v_j^2(\boldsymbol{0})\rangle\right]^{1/2}}\,, \tag{5}$$

where $\boldsymbol{0}$ is an arbitrary origin point used to normalize the velocity correlations, we can express equation (4) as

$$\langle v_i(\boldsymbol{a})\,v_j(\boldsymbol{b})\rangle_m = \frac{\left[\langle v_i^2(\boldsymbol{0})\rangle\langle v_j^2(\boldsymbol{0})\rangle\right]^{1/2}}{L^4}\int_{D_a}\int_{D_b}R_{ij}(\boldsymbol{a}+\boldsymbol{x},\boldsymbol{b}+\boldsymbol{x'})\,\mathrm{d}\boldsymbol{x}\mathrm{d}\boldsymbol{x'} + \\ + \langle \epsilon_i(\boldsymbol{a})\,\epsilon_j(\boldsymbol{b})\rangle\,. \tag{6}$$

Equation (6) is general and can be applied to non-homogeneous PIV measurement conditions, once the two-point correlation R_{ij} is known, measured or extrapolated.

A change of variables can now be introduced as $(\boldsymbol{x},\boldsymbol{x'}) \to (\boldsymbol{\xi},\boldsymbol{r}) = (\boldsymbol{x},\boldsymbol{x'}-\boldsymbol{x})$. Assuming that the flow field is statistically homogeneous in the image plane (a local homogeneity suffices) allows us to rewrite equation (6) in terms of separation vectors, namely $\boldsymbol{r} \equiv \boldsymbol{q}-\boldsymbol{p}$ and $\boldsymbol{s} \equiv \boldsymbol{b}-\boldsymbol{a}$. Local planar homogeneity indicates that $R_{ij}(\boldsymbol{r}) = R_{ji}(-\boldsymbol{r})$, and allows us to simplify equation (6) to

$$\langle v_i(\boldsymbol{0})\,v_j(\boldsymbol{s})\rangle_m = \frac{\left[\langle v_i^2\rangle\langle v_j^2\rangle\right]^{1/2}}{L^4}\left\{\left[\int_0^L (L-r_1) + \int_{-L}^0 (L+r_1)\right]\right. \\ \left.\left[\int_0^L (L-r_2) + \int_{-L}^0 (L+r_2)\right] R_{ij}(\boldsymbol{s}+\boldsymbol{r})\,\mathrm{d}r_1\mathrm{d}r_2\right\} + \sigma_\epsilon^2\delta_{ij}H(|\boldsymbol{s}|)\,, \tag{7}$$

where subscripts 1 and 2 indicate the two in-plane components of separation vector $\boldsymbol{r}$, δ_{ij} is the Kronecker delta and $H(s) = 1$ if $s = 0$ and zero otherwise. Equation (7) indicates that, for a given flow, the effect of spatial filtering on the measured $\langle v_i(\boldsymbol{0})\,v_j(\boldsymbol{s})\rangle$ depends on the unfiltered two-point correlation tensor $R_{ij}(\boldsymbol{r})$, while the noise effect will be perceived only in the variances when $\boldsymbol{s} = \boldsymbol{0}$. Equation (7) is the most general statement of PIV's filter effect on two-point covariance in the special case of homogeneous flow, expressed for the first time in physical space. Once the two-point correlation is known, equation (7) can be integrated providing all the needed information about the spatial averaging effects.

In the special case of homogeneous isotropic turbulence R_{ij} can be expressed as (Batchelor, 1953)

$$R_{ij}(\boldsymbol{r}) = g(r)\,\delta_{ij} + [f(r) - g(r)]\,\frac{r_i r_j}{r^2}\,, \tag{8}$$

where $r = \left(r_1^2 + r_2^2 + r_3^2\right)^{1/2}$ and $f\left(r\right)$ and $g\left(r\right)$, for incompressible flows, are functions related by the identity

$$g\left(r\right) = f\left(r\right) + \frac{r}{2}\frac{\mathrm{d}f}{\mathrm{d}r}. \tag{9}$$

With this assumption, in the special case of $\boldsymbol{s} = \mathbf{0}$ and $i = j = 1$, equation (7) becomes similar to the expression reported by Dryden et al (1937) to quantify spatial filtering effects for hot-wire anemometry (although here generalized for a two-dimensional domain)

$$\left\langle v_1^2 \right\rangle_m = \frac{4\left\langle v_1^2\right\rangle}{L^4}\int_0^L\int_0^L \left(L - r_1\right)\left(L - r_2\right) R_{11}\left(\boldsymbol{r}\right)\mathrm{d}r_1\mathrm{d}r_2 + \sigma_\epsilon^2. \tag{10}$$

We now use a polynomial approximation for $f\left(r\right)$ in the limit $r \ll \lambda_f$, where λ_f is the longitudinal Taylor microscale defined by $\lambda_f^{-2} = -\mathrm{d}^2 f/\mathrm{d}r^2\left(0\right)/2$ (Batchelor, 1953)

$$f\left(r\right) = 1 - \frac{r^2}{\lambda_f^2} \longrightarrow g\left(r\right) = 1 - \frac{2r^2}{\lambda_f^2} \longrightarrow R_{ij}\left(\boldsymbol{r}\right) = \delta_{ij} + \frac{r_i r_j - 2\delta_{ij}r^2}{\lambda_f^2}. \tag{11}$$

By substituting equation (11) into (7) we obtain

$$\frac{\left\langle v_1\left(\mathbf{0}\right) v_1\left(\boldsymbol{s}\right)\right\rangle_m}{\left\langle v_1^2\right\rangle} \approx 1 - \frac{2s_1^2 + 4s_2^2 + L^2}{2\lambda_f^2} + \frac{\sigma_\epsilon^2}{\left\langle v_1^2\right\rangle} H\left(\left|\boldsymbol{s}\right|\right), \tag{12}$$

and

$$\frac{\left\langle v_1\left(\mathbf{0}\right) v_2\left(\boldsymbol{s}\right)\right\rangle_m}{\left\langle v_1^2\right\rangle} \approx \frac{s_1 s_2}{\lambda_f^2}, \tag{13}$$

where s_1 and s_2 indicate the magnitude of the components of $\boldsymbol{s}$ in the directions 1 and 2 belonging to the image plane (namely $\boldsymbol{s} = \left(s_1, s_2\right)$).

Equation (12) demonstrates that the two-point correlation $\left\langle v_1\left(\mathbf{0}\right) v_1\left(\boldsymbol{s}\right)\right\rangle_m$ is indeed affected by the spatial resolution used in the experiment, while the off-diagonal term $\left\langle v_1\left(\mathbf{0}\right) v_2\left(\boldsymbol{s}\right)\right\rangle_m$ is not, at least for small L and s. It follows from equation (13) that in isotropic conditions, the measured Reynolds stress is still zero. More interestingly, the ratio between the measured and the actual variance is

$$\frac{\left\langle v_1^2\right\rangle_m}{\left\langle v_1^2\right\rangle} \approx 1 - \frac{L^2}{2\lambda_f^2} + \frac{\sigma_\epsilon^2}{\left\langle v_1^2\right\rangle}. \tag{14}$$

Equation (14) provides a straightforward estimate of the attenuation of the measured variance compared to the real one as a function of the window size, L, compared to the Taylor microscale, λ_f. However, if $L/\lambda_f \geq O(1)$ (for instance when characterizing wall-parallel planes in a turbulent boundary layer) equation (14) is not accurate due to the failure of the polynomial approximation, and equation (10) should be preferred together with an opportune ansatz of the two-point correlation.

We then examine the effect of the spatial resolution on the second-order structure functions defined as

$$\begin{aligned} D_{ij,m}\left(\boldsymbol{s}\right) &= \left\langle\left[v_i\left(\boldsymbol{s}\right) - v_i\left(\mathbf{0}\right)\right]\left[v_j\left(\boldsymbol{s}\right) - v_j\left(\mathbf{0}\right)\right]\right\rangle_m = \\ &= 2\left\langle v_i v_j\right\rangle_m - \left\langle v_i\left(\mathbf{0}\right) v_j\left(\boldsymbol{s}\right)\right\rangle_m - \left\langle v_i\left(\mathbf{0}\right) v_j\left(-\boldsymbol{s}\right)\right\rangle_m. \end{aligned} \tag{15}$$

According to equations (12) and (13), the attenuation of the longitudinal and transverse structure functions becomes

$$\frac{D_{11,m}}{\langle v_1^2\rangle} \approx \frac{2s_1^2+4s_2^2}{\lambda_f^2} + 2\frac{\sigma_\epsilon^2}{\langle v_1^2\rangle}\left[1-H\left(|\boldsymbol{s}|\right)\right] \qquad \text{and} \qquad \frac{D_{12,m}}{\langle v_1^2\rangle} \approx -\frac{2s_1s_2}{\lambda_f^2}\,, \tag{16}$$

namely they are unaffected by spatial resolution, at least in the limit of $s \ll \lambda_f$ and $L \ll \lambda_f$.

All of these results are only valid in the limit of small L/λ_f, but this does not diminish their utility, as PIV measurements typically have $L/\lambda_f \ll 1$. The range of applicability of equation (7) can also be extended by adopting alternative analytical expressions for the correlation tensor $R_{ij}(\boldsymbol{r})$ (in homogeneous flows) or of the correlation function $f(r)$ only (in homogeneous and isotropic flows). However, these expressions are typically more complex than equation (11) and seldom allow for an analytical solution. As a consequence, the integral (7) should be computed numerically as discussed in section 5.

3 Numerical methodology

A numerical data set has been obtained from Direct Numerical Simulation (DNS) by using a classical pseudo-spectral method. The Navier-Stokes equations have been integrated in a triperiodic domain of length $L_D = 2\pi$ using a Fourier spectral method with the nonlinear terms de-aliased by the 3/2 rule. The time integration is performed with a third-order low-storage Runge-Kutta method (Lundbladh et al, 1992). The nonlinear terms are computed using an Adam-Bashforth approximation while the diffusive terms are integrated analytically (Rogallo, 1981). A random forcing is applied isotropically to the first shell of wave vectors, with fixed amplitude $\hat{f}_0$, constant in time and uniformly distributed in phase and directions (Vincent and Meneguzzi, 1991). A resolution of $192\times192\times192$ Fourier modes in the three directions, that corresponds to a grid size in physical space of $288\times288\times288$ collocation points due to de-aliasing, is used. The Taylor Reynolds number of the present simulations is $Re_\lambda = \sqrt{2k/3}\,\lambda/\nu = 150$, where k is the turbulent kinetic energy and λ is the Taylor microscale. The ratio between the highest resolved wave number $\kappa_{\max}$ and the Kolmogorov wave number κ_η is $\kappa_{\max}/\kappa_\eta = 1.73$, which is within the usual accepted range to ensure stability and sufficient resolution to simulate dynamics accurately (Pope, 2000). For the statistics, about 80 independent and identically distributed velocity fields are used (one is stored each eddy turn-over time t_0).

The time history of the turbulent kinetic energy, k, and of the turbulent dissipation, ϵ, integrated over the whole domain, is shown in the left panel of figure 1. These characteristic observables of homogeneous isotropic turbulence are known to be subject to strong fluctuations around their mean value. The data in the figure illustrate that the simulation was run long enough to capture these characteristic cycles, especially for the observables that are most sensitive to large-scale motions, such as the turbulent kinetic energy. The right panel of figure 1 shows the power spectral density of the turbulent kinetic energy from the DNS. The wave numbers have been normalized with the Kolmogorov scale $\eta = (\nu^3/\epsilon)^{1/4}$, where ν is the kinematic viscosity of the flow. The spectrum in figure 1 shows also an inertial subrange with a power-law slope over about one wavenumber decade, as expected for

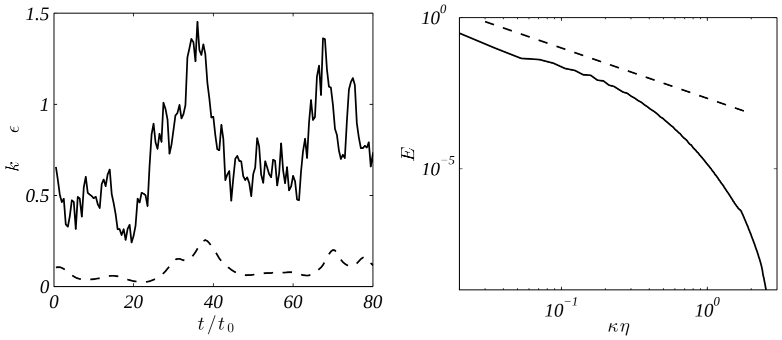

Fig. 1 Left panel: Time history of the turbulent kinetic energy k (solid line) and turbulent dissipation ϵ (dashed line). Right panel: spectra of the turbulent kinetic energy versus wave number normalized with the Kolmogorov length scale, η. The dashed line is proportional to the Kolmogorov spectral law, $E \propto \kappa^{-5/3}$.

Turbulent kinetic energy	$k = \overline{(u_{\mathrm{rms}}^2 + v_{\mathrm{rms}}^2 + w_{\mathrm{rms}}^2)}/2$	4.45 [$\times 10^{-4}$ m^{2}s^{-2}]
	$u_t = \sqrt{2k/3}$	1.72 [$\times 10^{-2}$ ms^{-1}]
Longitudinal integral length scale	Λ_x	31.0 [$\times 10^{-3}$ m]
Taylor microscale	λ_x	8.86 [$\times 10^{-3}$ m]
Eddy turnover time	$T = \Lambda_x/u_t$	1.8 [s]
Dissipation rate (from λ_x)	$\epsilon = 15\nu\ u_t^2/\lambda_x^2$	4.6 [$\times 10^{-5}$ m^{2}s^{-3}]
Kolmogorov time scale	$\tau_\eta = (\nu/\epsilon)^{1/2}$	0.14 [s]
Kolmogorov length scale	$\eta = (\nu^3/\epsilon)^{1/4}$	0.38 [$\times 10^{-3}$ m]
Reynolds number (based on Λ_x)	$\mathrm{Re}_L = (\Lambda_x u_t)/\nu$	534
Reynolds number (based on λ_x)	$\mathrm{Re}_\lambda = (\lambda_x u_t)/\nu$	153

Table 1 Flow statistics from the Direct Numerical Simulation.

this Reynolds number (Pope, 2000). A summary of the main turbulent statistics extracted from the simulation is given in table 1. The numerical value are obtained by matching the dissipation and the kinematic viscosity between the simulation and the experiment described in section 4.

In order to replicate the PIV filtering effect (and the corresponding effect on the turbulence statistics), the flow field has been filtered following the definition of the filter given in equation (1). For simplicity, we only report here the expression for the one-dimensional case. The filtered velocity in the point i can be written in terms of grid parameters as

$$V_m(x_i) = \frac{1}{L_x}\int_{x_i-0.5N\Delta x}^{x_i+0.5N\Delta x} V(x)\mathrm{d}x\,, \tag{17}$$

where Δx is the grid spacing and N is the (even) number of grid points in the filter domain. We then perform the numerical integration with the trapezoidal rule, defined as

$$V_m(x_i) = \frac{V(x_i - 0.5N\Delta x) + V(x_i + 0.5N\Delta x)}{2N} + \sum_{j=-N/2+1}^{N/2-1} \frac{V(x_i + j\Delta x)}{N}\,. \tag{18}$$

In the two-dimensional case, the trapezoidal rule is applied two times in both of the two directions that define the observation plane.

Turbulent kinetic energy	$k = \overline{(u_{\rm rms}^2 + v_{\rm rms}^2 + w_{\rm rms}^2)}/2$	6.07 ± 0.6 [$\times 10^{-4}$ m^{2}s^{-2}]
	$u_t = \sqrt{2k/3}$	2.01 ± 0.1 [$\times 10^{-2}$ ms^{-1}]
Longitudinal integral length scale	Λ_x	95.0 ± 0.5 [$\times 10^{-3}$ m]
Taylor microscale	λ_x	11.4 ± 0.5 [$\times 10^{-3}$ m]
Eddy turnover time	$T = \Lambda_x/u_t$	4.7 ± 0.2 [s]
Dissipation rate (from λ_x)	$\epsilon = 15\nu\ u_t^2/\lambda_x^2$	4.6 ± 0.5 [$\times 10^{-5}$ m^{2}s^{-3}]
Kolmogorov time scale	$\tau_\eta = (\nu/\epsilon)^{1/2}$	0.14 ± 0.01 [s]
Kolmogorov length scale	$\eta = (\nu^3/\epsilon)^{1/4}$	0.38 ± 0.01 [$\times 10^{-3}$ m]
Reynolds number (based on Λ_x)	$\mathrm{Re}_L = (\Lambda_x u_t)/\nu$	1977 ± 100
Reynolds number (based on λ_x)	$\mathrm{Re}_\lambda = (\lambda_x u_t)/\nu$	237 ± 25

Table 2 Flow statistics from single-phase measurements (the uncertainties correspond to the 95% confidence intervals). The integral length scale and the Taylor microscale are computed from the longitudinal two-point correlation; the dissipation rate and the Kolmogorov scales are computed from λ_x using the definitions given in Pope (2000).

4 Experimental setup

Laboratory experiments are performed in a stirred tank of dimensions $800 \times 800 \times 3600$ mm^3. The tank is filled with tap water, which is initially filtered to 5 μm and purified by a flow-through ultraviolet filter when experiments are not being run. Stirring is provided by two jet arrays symmetrically located with respect to the vertical center-plane of the tank, at a distance of $\pm$810 mm from the center. Each array is made of 8×8 synthetic jets, which are actuated following a stochastic algorithm. The algorithm is designed to maximize turbulent production while minimizing the mean flow in the tank, as described by Variano and Cowen (2008). Due to the symmetric configuration of the jet arrays, the resulting flow is homogeneous and isotropic in a large (about 3 integral length-scales) region at the center of the tank (see Bellani and Variano, 2014, for a detailed report on the flow quality). The integral length-scale of the present experimental data, Λ_x, is 95 mm while the Taylor length scale, λ_x, is 11.4 mm. The Reynolds number based on the Taylor length scale is $\mathrm{Re}_\lambda = 237$ (see table 2).

Measurements are performed in the homogeneous and isotropic region using 2D-PIV. We use one 12-bit CCD camera with an 1600×1200 array of 7.4 μm pixels (Imager PRO-X), and fitted with a 105 mm lens (Nikkor). The laser light sheet (frequency-doubled Nd-YAG) is 1 mm thick, with tracer particles of size 10 μm (silver coated glass spheres). The measurement plane is vertical and oriented along the longest dimension of the tank. In this plane, we focus on a 35×47 mm^2 area centered at the tank center. To compute the velocity fields, we use the commercial software Davis 7.2 from LaVision GmbH, which implements continuous window deformation and reduction (for a detailed report on algorithm performance see Stanislas et al, 2005). We report the main PIV operating parameters in table 3. The final size of the interrogation window is 32×32 pixels with 50% overlap and a square weighting function. This gives a vector spacing of 0.44 mm in physical space, and a physical size of the interrogation area of 0.88 mm, which is about twice the Kolmogorov length scale for this flow. Thus the resolution is fine enough to resolve more than 99% of the turbulent kinetic energy (Saarenrinne et al, 2001).

Particular care was taken to minimize the noise level, which can greatly affect the measurements of turbulent quantities like Taylor microscale. For this reason, we removed (but not replaced) outliers using a 3×3 median test. The number

Interrogation area	IA	[pixels × pixels]	32 × 32
Interrogation area	IA	[mm × mm]	0.88 × 0.88
Vector spacing	dx, dy	[mm]	0.44
Time between laser pulses	dt	[$\times 10^{-1}$ s]	0.15
Average displacement	$u_t dt$	[$\times 10^{-3}$ m]	0.26

Table 3 Summary of present PIV settings.

of outliers was below 5% of the total number of vectors. The amount of residual noise is estimated using the methodology proposed by Poelma et al (2006), and found it to be below 1% of u_t.

To provide the coarse-resolution datasets, we filtered the original, well-resolved data according to the definition (1) with windows of varying size. The integral in equation (1) is solved numerically using the trapezoid rule described by equation (18). One and two-point statistics are then computed from the filtered datasets. The velocity covariance $\langle v_1 v_2 \rangle_m$ was calculated from the experimental data and it was found to be nearly zero (less than 0.03 when normalized by the velocity variance) with a negligible variation with L. All statistics are computed from 1700 independent and identically distributed PIV snapshots.

5 Results

As discussed in section 2, under HIT conditions the two-point correlation tensor, $R_{ij}(\boldsymbol{r})$, is completely defined by the longitudinal correlation function, $f(r)$. Once $f(r)$ is known, we can compute the effect of the spatial resolution on the measured variance, $\langle v_1^2 \rangle_m$, and on the structure functions, $D_{ij,m}(\boldsymbol{s})$, using equations (7) and (15). Here and in the following it will be assumed that the effect of measurement-noise has been removed from the autocorrelation function, for instance by following the approach of Poelma et al (2006). Figure 2 shows the longitudinal correlation function, $f(\hat{r})$, where $\hat{r} = r/\lambda_f$, from the experimental and numerical datasets. Here and in the following figures the Taylor microscale is determined by using equation (20) with the highest resolution data. Both datasets agree for small $\hat{r}$ with the polynomial approximation $f(\hat{r}) \approx 1 - \hat{r}^2$, but they deviate significantly from it already at $\hat{r} \approx 0.4$. Therefore, an empirical function was used to fit the correlation functions as

$$f(\hat{r}) = \exp\left(-\frac{\hat{r}^2}{1 + A\hat{r}^B}\right), \tag{19}$$

where the constants A and B are determined by fitting the longitudinal correlation function with (19). Equation (19) is consistent with the polynomial approximation in the limit of small $\hat{r}$ and therefore has been preferred to other expressions found in literature (see Pope, 2000, for instance). Due to differences in Reynolds number and large-scale forcing, the experimental and numerical datasets show different correlation function shapes. Hence we obtain two sets of fitting parameters, namely $A = 4.46$ and $B = 1.31$ for the experimental data and $A = 2.58$ and $B = 1.47$ for the numerical data. The two empirical curves in figure 2 fit the data reasonably well, and thus we use them to calculate the two-point correlation tensor (8), and subsequently the integrals in equations (7) and (10).

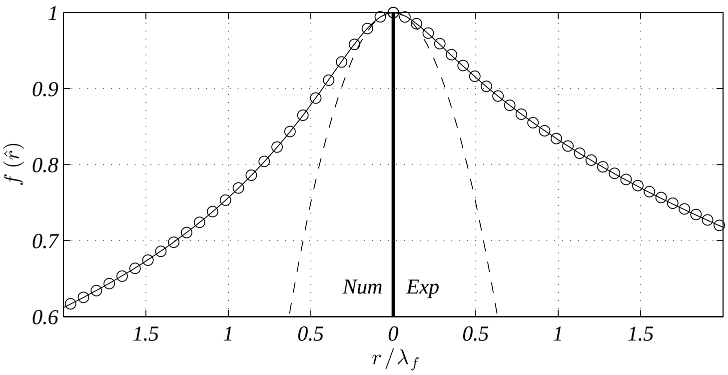

Fig. 2 Comparison between the numerical/experimental longitudinal correlation function, $f(\hat{r})$, with the used ansazt (19) (solid line) and the polynomial formula $f(\hat{r}) = 1-\hat{r}^2$ commonly used to approximate it at small r-values (dashed line). Numerical and experimental datasets are shown on left and right panel, respectively.

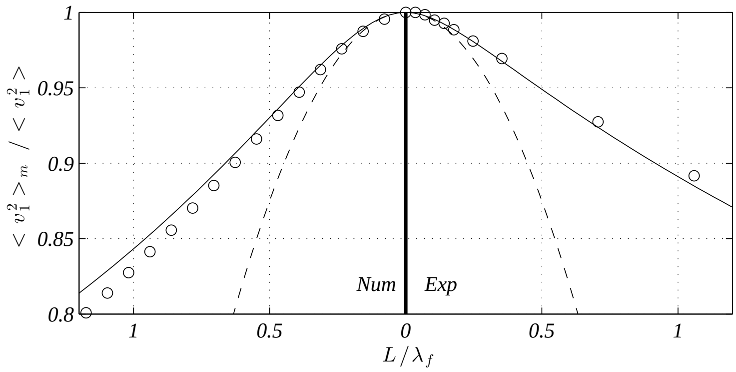

Fig. 3 Comparison between the numerical and experimental velocity variance attenuation for different filter sizes L/λ_f. The solid line is the attenuation predicted by the integration of equation (10) with the ansazt (19), while the dashed line is equation (14), namely the simple polynomial model valid for $L \ll \lambda_f$.

5.1 Attenuation of two-point statistics

Figure 3 shows the attenuation of the measured variance as function of L/λ_f. It is possible to see that the theory is able to capture the effects of spatial filtering, provided that we use the appropriate form of the correlation function. For $L/\lambda_f < 0.1$, which is representative of many PIV applications, spatial filtering effects are well described by the polynomial approximation we propose in equation (14). In this range, the attenuation is relatively weak ($< 5\%$) but stronger than in the corresponding 1-D case (for instance in hot-wire anemometry, as discussed by Segalini et al, 2011b). In some applications (*e.g.* high-Reynolds number flows) L/λ_f can become quite large (> 1) as λ_f becomes smaller. In this range, the attenuation becomes more severe (e.g. exceeding 10%). In this case, correction schemes based on the empirical fit are essential.

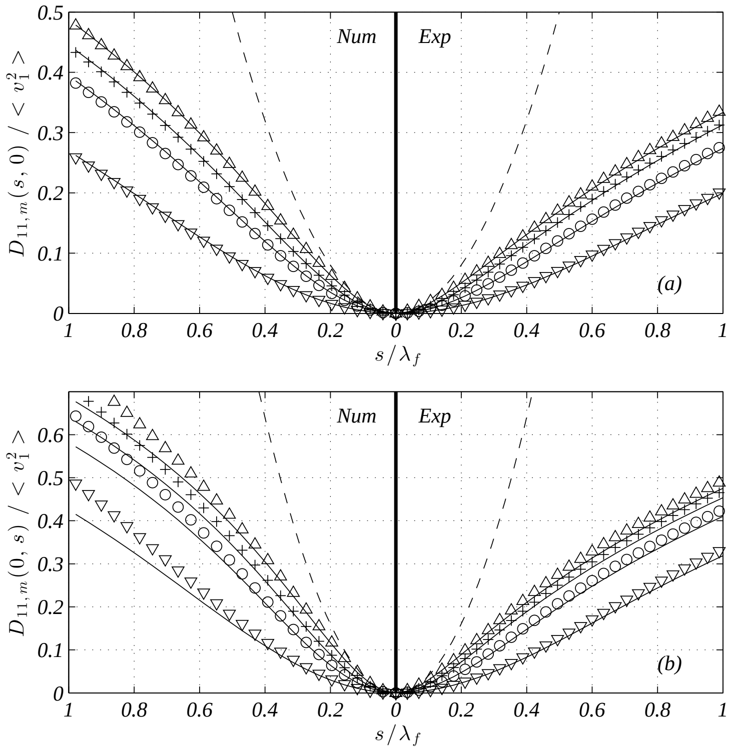

Fig. 4 Comparison between longitudinal (a) and transverse (b) structure functions. ($\triangle$) $L/\lambda_f \approx 0$, ($+$) $L/\lambda_f \approx 0.21$, ($\bigcirc$) $L/\lambda_f \approx 0.38$, ($\triangledown$) $L/\lambda_f \approx 0.78$. The solid lines are the theoretical attenuations (computed by means of equations (7), (15) and (19)) while the dashed lines are obtained from equation (16).

The longitudinal and transverse structure functions are reported in figure 4 for different separation distances and filter scales. As shown in the figure, our proposed polynomial approximation (16) is able to describe the evolution of the structure functions for small separations ($s/\lambda_f < 0.2$) and very small filter sizes ($L/\lambda_f < 0.15$). The deviation from it increases with s/λ_f and L/λ_f and a better approximation is provided by the theory described in section 2 with the correlation function described by (19), as shown in the figure.

Second order structure functions are often used in experiments to estimate the turbulent kinetic energy dissipation rate, ε, according to the Kolomogorov hypothesis (Sreenivasan, 1984; Saddoughi and Veeravalli, 1994; Gibert et al, 2010; Bellani et al, 2012). For separation distances, $\boldsymbol{s} = (s, 0)$, belonging to the inertial subrange, Kolmogorov (1941) predicted the scaling $D_{11}(\boldsymbol{s}) = C(\varepsilon s)^{2/3}$, where C is believed to be a universal constant (Sreenivasan, 1995). Figure 5 shows the longitudinal structure function scaled according to Kolmogorov hypothesis. The figure demonstrates that the structure function reaches a plateau for $s/\lambda_f > 1$ (this is especially evident in the experimental dataset, as the Reynolds number is higher than in the DNS case). Figure 5 also shows that spatial filtering effects have a strong influence on the height of this plateau. In particular, we see that the

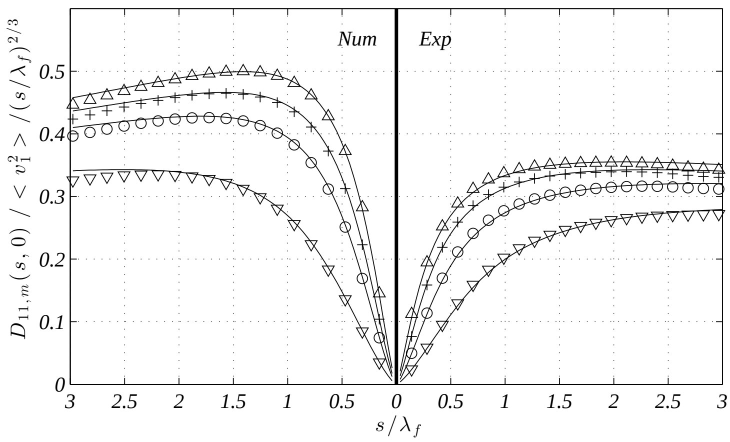

Fig. 5 Longitudinal structure functions scaled according to Kolmogorov hypothesis. ($\triangle$) $L/\lambda_f \approx 0$, ($+$) $L/\lambda_f \approx 0.21$, ($\bigcirc$) $L/\lambda_f \approx 0.38$, ($\triangledown$) $L/\lambda_f \approx 0.78$. The solid lines are estimated as in figure 4.

dissipation rate is under-estimated for increasing filter size. Strategies to correct this bias using the error models are discussed below.

5.2 Measured Taylor microscale

As noted in the previous section, the ratio L/λ_f plays a crucial role in the attenuation of the velocity variance. However, since this length scale is also estimated from the available filtered data, it is expected that it will suffer from the spatial resolution error of the PIV images. Therefore, it is interesting to see how the measured $\lambda_{f,m}$ varies with the filter scale L. From a theoretical point of view, the value $\lambda_{f,m}$ can be obtained in two steps: i) computing the filtered correlation functions by integrating equation (7) with the ansazt (19); ii) taking the second derivative of the filtered autocorrelation function at the origin

$$\lambda_{f,m}^{-2} = -\frac{1}{2\left\langle v_1^2\right\rangle_m}\frac{\mathrm{d}^2}{\mathrm{d}s^2}\left\langle v_1\left(\mathbf{0}\right)v_1\left(s\boldsymbol{e}_1\right)\right\rangle_m = \frac{1}{4\left\langle v_1^2\right\rangle_m}\frac{\mathrm{d}^2}{\mathrm{d}s^2}\left[D_{11,m}\left(s\boldsymbol{e}_1\right)\right]\,. \qquad (20)$$

Figure 6 shows the comparison between the theoretical values and the ones measured from the numerical and experimental datasets. The data and theory indicate a nearly linear growth of $\lambda_{f,m}$ with increasing L/λ_f owing to the increased correlation at large scales in the filtered field.

Finally, we look at the structure functions normalized with the measured Taylor microscale, $\lambda_{f,m}$, and the measured variance, $\left\langle v_1^2\right\rangle_m$, as shown in figure 7. This figure is interesting as in a real experiment, λ_f and $\left\langle v_1^2\right\rangle$ are initially unknown. This normalization forces the structure functions to collapse near the origin (following from the definition of $\lambda_{f,m}$, derived by fitting a parabola through f). However, for $s > 0.3\lambda_{f,m}$ the deviations induced by the filter become evident and the structure functions increase when increasing the filter width, unlike the case in figure 4, where a decrease was evident under the same conditions. The difference between

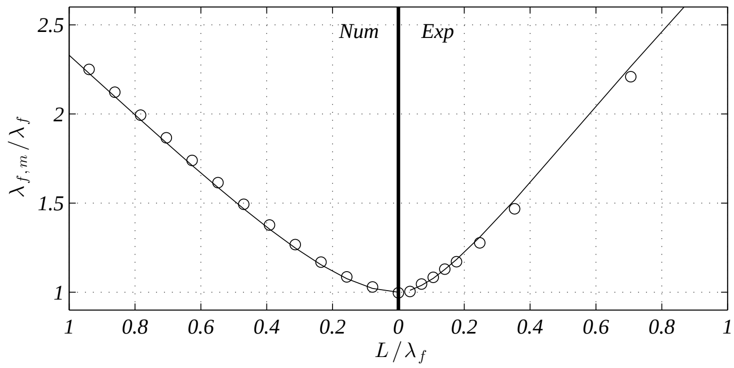

Fig. 6 Comparison between the numerical and experimental Taylor microscale for different filter scales L/λ_f estimated by means of equation (20). The solid lines show the theoretical curved obtained by the integration of equation (7) with the ansazt (19).

the structure functions obtained with different filter widths, L, are anyway smaller that those shown in figure 4. This suggests that scaling the structure functions with the measured variance and Taylor microscale better compensates for a limited spatial resolution, analogously to what observed for the velocity flatness measured with hot-wire anemometry (Talamelli et al, 2013).

5.3 Estimation of the corrected velocity variance and Taylor microscale

In the previous section, we have described the effect of the finite size of the PIV interrogation window. It is of interest now to understand whether or not this can be used to correct the measured two-point statistics. This can be accomplished by following the idea proposed by Segalini et al (2011b), who used the data measured by two hot-wire anemometers of different lengths to improve the accuracy of the measured velocity variance and to estimate the Taylor microscale. Similarly, two interrogation windows can be used to analyze the PIV data (with window size L_1 and L_2) and two different velocity statistics can be obtained (named $\langle v_1^2 \rangle_{m1}$ and $\langle v_1^2 \rangle_{m2}$, respectively).

This is checked here by the following procedure: two datasets are chosen with different interrogation-window sizes (with $L_1 < L_2$) and the longitudinal correlation function, $f(r)$, for the first data set is calculated. This allows the determination of the constants A and B in equation (19). Consequently, the two-point correlation is known from equation (8) and equation (10) providing an estimate of the variance attenuation of the form $\langle v_1^2 \rangle_m = \langle v_1^2 \rangle F(L/\lambda_f)$. The unfiltered velocity variance and the Taylor microscale can be determined by solving the nonlinear system

$$\begin{cases} \langle v_1^2 \rangle_{m1} = \langle v_1^2 \rangle F(L_1/\lambda_f) \\ \langle v_1^2 \rangle_{m2} = \langle v_1^2 \rangle F(L_2/\lambda_f) \end{cases} . \tag{21}$$

Figure 8 shows the relative error obtained using the available data. The relative error is defined as the difference between the estimated value and the real value (measured for the smallest window size) normalized by the real value. Consider

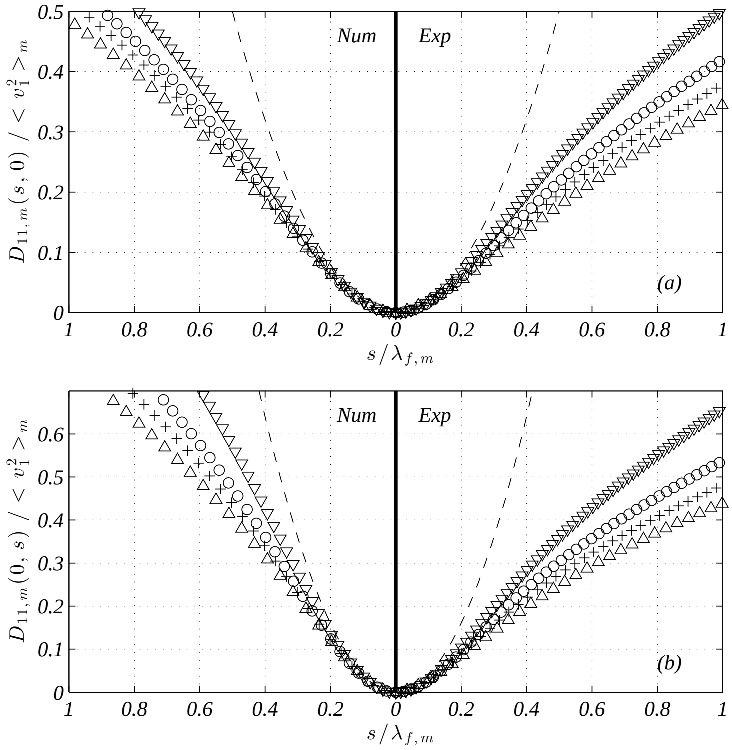

Fig. 7 Comparison between the numerical (left) and experimental (right) longitudinal (a) and transverse (b) structure functions normalized with the measured Taylor microscale, $\lambda_{f,m}$, and measured variance, $\langle v_1^2 \rangle_m$. ($\triangle$) $L/\lambda_f \approx 0$, (+) $L/\lambda_f \approx 0.21$, ($\bigcirc$) $L/\lambda_f \approx 0.38$, ($\triangledown$) $L/\lambda_f \approx 0.78$. The dashed lines are obtained from the polynomial expression (16).

first that, according to figures 3 and 6, the measured velocity variance and Taylor microscale can change by 10% and 150%, with respect to the case with $L \approx 0$ for $L \approx \lambda_f$. The figure indicates that the present methodology is beneficial as it reduces the effects of spatial averaging significantly. The results depend on the particular combination of L_1 and L_2 but, as long as a realistic L_1 is used, any L_2-filtered data set can be adopted to improve the measured statistics. This is particularly evident for the velocity variance, while the Taylor microscale is less robust, similarly to what was noticed by Segalini et al (2011b).

6 Conclusions

In this work a theoretical framework to estimate 2-D filtering effects on the statistics of a homogenous turbulent flow field is proposed. This methodology can be used to evaluate the effect of limited resolution on second-order statistical quantities measured by Particle Image Velocimetry (where two-dimensional spatial filtering of the velocity field is introduced by the finite size of the interrogation area); it can be easily extended providing a consistent mathematical framework to correct turbulence statistics measured with insufficient resolution, similarly to what done

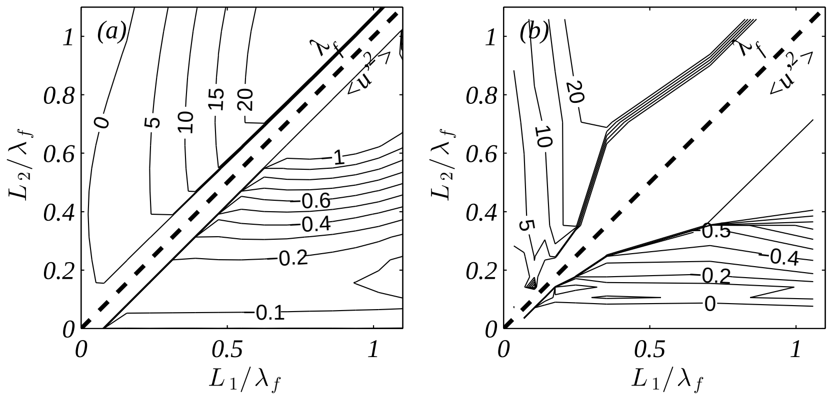

Fig. 8 Comparison of the percentual relative error in the estimated velocity variance (*lower corner*) and Taylor microscale (*upper corner*) from two measurements with different window size (L_1 and L_2). (*a*) Numerical data and (*b*) experimental data.

by Segalini et al (2011b) and Talamelli et al (2013) in hot-wire anemometry. The present theory is based on the idea of an analogous linear spatial filter, which is justified in the appendix. For the special case of homogeneous isotropic flows, simple relationships between the averaged and non-averaged two-point correlations can be obtained, providing an estimation of the effect of window size in the measured statistics.

It is demonstrated that spatial-filtering effects in the second-order statistics are strictly related to properties of the two-point correlation tensor, and to the ratio L/λ_f, where L is the filter scale and λ_f is the Taylor length scale. The knowledge of the two-point correlation function allows the correction of the second-order statistics in flows that are homogeneous in the image plane, for instance turbulent boundary layers with image planes parallel to the wall. In order to validate the theory, experimental and numerical two-point velocity statistics of homogeneous and isotropic turbulence have been used. It has been observed that for small L/λ_f ($L/\lambda_f < 0.3$) the velocity variance attenuation is less than 5% and a straightforward correction scheme can be obtained from the polynomial approximation of the two-point correlation that accounts only for the Taylor microscale. For larger separation distances, the use of an exponential function to model the unfiltered two-point correlation improves the agreement between the theory and the datasets, demonstrating that the model based on the exponential function (and the theoretical framework in general) is able to capture the attenuation of velocity variance as well as the change of the second-order structure functions.

The correction scheme proposed here can be used in at least two ways. The first (direct) way allows the determination of the measured statistics starting from the true ones. This is useful for instance in the validation of numerical schemes (that may or may not suffer the spatial resolution problem) against filtered experimental data, allowing for a fair comparison of the two. The second (inverse) way to use our results is to identify, model, and remove the spatial resolution error in experimental data. Doing so may require an iterative approach, given that the estimation of the model input (Taylor length scale) is itself dependent on the model output. An alternative correction strategy follows the idea of Segalini et al (2011b). By using the measured statistics from the same flow filtered with two different spatial filters, one can determine the corrected velocity variance and Taylor microscale. In a practical situation one could use the most resolved field and another field obtained by doubling the interrogation window size: known the two interrogation window sizes and the relationship $\langle v^2 \rangle_m = \langle v^2 \rangle G(L/\lambda_f)$ it is indeed possible to obtain an unfiltered estimate of $\langle v^2 \rangle$ and λ_f. This approach has been applied to demonstrate an improved estimation of the velocity variance, whereas the estimation of the Taylor microscale turns out to be not as robust as the correction of the variance.

A Relationship between interrogation window and measured velocity

To quantify the effect of the interrogation window on the measured velocity, let us consider two PIV images taken at two different instants t_0 and $t_1 = t_0 + \Delta t$. It is expected that these images will be black (zero light intensity) almost everywhere, with the exception of some points where the laser light reflected by the particles is detected. We assume now a square interrogation area, I_0, of size L where N particles are located in the first image, and another interrogation area in the second image, I_1, of the same size as I_0 but translated with a convection velocity $\boldsymbol{V}_m$, for the moment undefined. The location of the illuminated points can be labelled as $\boldsymbol{x}_{0,i}$ in I_0 and $\boldsymbol{x}_{1,i} = \boldsymbol{x}_{0,i} + (\boldsymbol{V}_i - \boldsymbol{V}_m)\,\Delta t$ in I_1 with $i \in \{1, 2, ..., N\}$, where $\boldsymbol{V}_i$ denotes the average velocity of the i^{th}-particle between t_0 and t_1. It is assumed that there are only a negligible number of particles leaving the domain determined by the interrogation area, so that the present analysis has general validity. The light intensity distribution over the two interrogations areas can be expressed as

$$I_0(\boldsymbol{x}) = \sum_{i=1}^{N} \rho\,(\boldsymbol{x} - \boldsymbol{x}_{0,i}) \quad \text{and} \quad I_1(\boldsymbol{x}) = \sum_{i=1}^{N} \rho\,[\boldsymbol{x} - \boldsymbol{x}_{0,i} - (\boldsymbol{V}_i - \boldsymbol{V}_m)\,\Delta t]\ , \tag{22}$$

where $\rho(\boldsymbol{x})$ is a function that represents the light intensity around a particle located at the origin. For the sake of simplicity it will be assumed to be a rapidly decaying Gaussian.

The cross correlation operator between the two images can now be introduced as

$$R(\boldsymbol{\tau}) = \int_D I_0(\boldsymbol{x})\, I_1(\boldsymbol{x} + \boldsymbol{\tau})\, \mathrm{d}\boldsymbol{x}\,, \tag{23}$$

where D is a square domain of size L that includes the interrogation area. The cross-correlation, together with equation (22), becomes

$$R(\boldsymbol{\tau}) = \sum_{i=1}^{N}\sum_{j=1}^{N} \int_D \rho\,(\boldsymbol{x} - \boldsymbol{x}_{0,i})\, \rho\,[\boldsymbol{x} + \boldsymbol{\tau} - \boldsymbol{x}_{0,j} - (\boldsymbol{V}_j - \boldsymbol{V}_m)\,\Delta t]\, \mathrm{d}\boldsymbol{x}\,. \tag{24}$$

The maximum of the cross-correlation function identifies the optimal interrogation window displacement, $\boldsymbol{\tau}$, that ensures the highest correlation. Therefore $\boldsymbol{V}_m$ can be seen as the convective velocity maximizing $R(\mathbf{0})$. The maximum of the cross-correlation is readily obtained by imposing that the gradient must be zero at $\boldsymbol{\tau} = \mathbf{0}$ so that

$$\frac{\partial R}{\partial x_k} = \sum_{i=1}^{N}\sum_{j=1}^{N} \int_D \rho\,(\boldsymbol{x} - \boldsymbol{x}_{0,i})\, \frac{\partial \rho}{\partial x_k}\,[\boldsymbol{x} - \boldsymbol{x}_{0,j} - (\boldsymbol{V}_j - \boldsymbol{V}_m)\,\Delta t]\, \mathrm{d}\boldsymbol{x} = 0\,. \tag{25}$$

To proceed further it is possible to assume that the term $(\boldsymbol{V}_j - \boldsymbol{V}_m)\,\Delta t$ in equation (25) is small, so that a simple Taylor expansion can be used

$$\begin{aligned} \frac{\partial R}{\partial x_k} = \sum_{i=1}^{N}\sum_{j=1}^{N} \int_D \rho\,(\boldsymbol{x} - \boldsymbol{x}_{0,i})\, \frac{\partial \rho}{\partial x_k}\,(\boldsymbol{x} - \boldsymbol{x}_{0,j})\, \mathrm{d}\boldsymbol{x}\, - \\ - (\boldsymbol{V}_j - \boldsymbol{V}_m)_n\, \Delta t \int_D \rho\,(\boldsymbol{x} - \boldsymbol{x}_{0,i})\, \frac{\partial^2 \rho}{\partial x_k \partial x_n}\,(\boldsymbol{x} - \boldsymbol{x}_{0,j})\, \mathrm{d}\boldsymbol{x} = 0\,. \end{aligned} \tag{26}$$

The first integral is zero for $i = j$ since the function ρ is assumed to be isotropic, while for $i \neq j$ is approximately zero since it is assumed that no particles lie near the boundaries. The second integral is non-zero if $i = j$ and becomes negligible otherwise (since ρ is rapidly decaying). Therefore equation (26) can be approximated by considering only the second integral when $i = j$, and by noting that ρ is assumed to be the same for all particles

$$\int_D \rho\left(\boldsymbol{x} - \boldsymbol{x}_{0,1}\right) \frac{\partial^2 \rho}{\partial x_k \partial x_n} \left(\boldsymbol{x} - \boldsymbol{x}_{0,1}\right) \mathrm{d}\boldsymbol{x} \sum_{i=1}^{N} \left(\boldsymbol{V}_i - \boldsymbol{V}_m\right)_n = 0 \rightarrow \boldsymbol{V}_m = \frac{1}{N} \sum_{i=1}^{N} \boldsymbol{V}_i \,. \qquad (27)$$

The measured velocity is therefore the arithmetic mean of the average velocity (within Δt) of the N particles inside the interrogation area D.

Since the particles are assumed to be embedded in a velocity field $\boldsymbol{V}(\boldsymbol{x}, t)$ that is homogeneous in the image plane, they are uniformly distributed in space. The expected velocity of the generic i^{th}-particle inside D is statistically equal to the average flow velocity, assuming ideal particles with no inertia, therefore

$$\boldsymbol{V}_i = \frac{1}{L^2} \int_D \boldsymbol{V}(\boldsymbol{x}, t)\, \mathrm{d}\boldsymbol{x} \,, \qquad (28)$$

and the measured velocity can be expressed using equation (27) as

$$\boldsymbol{V}_m = \frac{1}{L^2} \int_D \boldsymbol{V}(\boldsymbol{x}, t)\, \mathrm{d}\boldsymbol{x} \,. \qquad (29)$$

In conclusion, the measured velocity is approximately equal to the integral average of the velocity field inside the interrogation area.

References

Adrian RJ (2005) Twenty years of particle image velocimetry. Exp Fluids 39:159–169

Batchelor GK (1953) The Theory of Homogeneous Turbulence. Cambridge University Press, Cambridge, UK

Bellani G, Variano EA (2014) Homogeneity and isotropy in a laboratory turbulent flow. Exp Fluids 55:1646

Bellani G, Byron ML, Collignon AG, Meyer CR, Variano EA (2012) Shape effects on turbulent modulation by large nearly neutrally buoyant particles. J Fluid Mech 712:41–60

Chen J, Katz J (2005) Elimination of peak-locking error in piv analysis using the correlation mapping method. Meas Sci Technol 16:1605

Dryden HL, Schubauer GB, Mock WC, Skramstad HK (1937) Measurements of intensity and scale of wind-tunnel turbulence and their relation to the critical Reynolds number of spheres. NACA Tech Rep 581

Foucaut JM, Carlier J, Stanislas M (2004) Piv optimization for the study of turbulent flow using spectral analysis. Meas Sci Technol 15:1046

Frenkiel FN (1949) The influence of the length of a hot wire on the measurements of turbulence. Phys Rev 75:1263–1264

Gibert M, Xu H, Bodenschatz E (2010) Inertial effects on two-particle relative dispersion in turbulent flows. EPL 90:64,005

Giordano R, Astarita T (2009) Spatial resolution of the stereo piv technique. Exp Fluids 46:643–658

Kähler CJ, Scharnowski S, Cierpka C (2012) On the resolution limit of digital particle image velocimetry. Exp Fluids 52:1629–1639

Kolmogorov A (1941) The local structure of turbulence in incompressible viscous fluid for very large reynolds numbers. Dokl Akad Nauk SSSR 30:299–303

Lavoie P, Avallone G, De Gregorio F, Romano GP, Antonia RA (2007) Spatial resolution of piv for the measurement of turbulence. Exp Fluids 43:39–51

Lundbladh A, Henningson DS, Johansson AV (1992) An efficient spectral integration method for the solution of the navier-stokes equations. FFA TN 28

Nobach H, Damaschke N, Tropea C (2005) High-precision sub-pixel interpolation in particle image velocimetry image processing. Exp Fluids 39:299–304

Poelma C, Westerweel J, Ooms G (2006) Turbulence statistics from optical whole-field measurements in particle-laden turbulence. Exp Fluids 40:347–363

Pope S (2000) Turbulent Flows. Cambridge University Press, Cambridge, UK

Raffel M, Willert CE, Wereley ST, Kompenhans J (2001) Particle image velocimetry. Spinger

Rogallo RS (1981) Numerical experiments in homogeneous turbulence. National Aeronautics and Space Administration

Saarenrinne P, Piirto M (2000) Turbulent kinetic energy dissipation rate estimation from piv velocity vector fields. Exp Fluids 29:S300–S307

Saarenrinne P, Piirto M, Eloranta H (2001) Experiences of turbulence measurement with piv. Meas Sci Technol 12:1904

Saddoughi SG, Veeravalli SV (1994) Local isotropy in turbulent boundary layers at high reynolds number. J Fluid Mech 268:333–372

Scarano F (2002) Iterative image deformation methods in piv. Meas Sci Technol 13

Scarano F (2003) Theory of non-isotropic spatial resolution in piv. Exp Fluids 35:268–277

Scarano F, Moore P (2012) An advection-based model to increase the temporal resolution of piv time series. Exp Fluids 52:919–933

Scarano F, Riethmuller ML (2000) Advances in iterative multigrid piv image processing. Exp Fluids 29:S051–S060

Scharnowski S, Hain R, Kähler CJ (2012) Reynolds stress estimation up to single-pixel resolution using piv-measurements. Exp Fluids 52:985–1002

Segalini A, Cimarelli A, Rüedi J, De Angelis E, Talamelli A (2011a) Effect of the spatial filtering and alignment error of hot-wire probes in a wall-bounded turbulent flow. Meas Sci Technol 22:105,408

Segalini A, Örlü R, Schlatter P, Alfredsson PH, Rüedi J, Talamelli A (2011b) A method to estimate turbulence intensity and transverse taylor microscale in turbulent flows from spatially averaged hot-wire data. Exp Fluids 51:693–700

Sreenivasan KR (1984) On the scaling of the turbulence energy dissipation rate. Phys Fluids 27(5):1048–1050

Sreenivasan KR (1995) On the universality of the kolmogorov constant. Phys Fluids 7(11):2778

Stanislas M, Okamoto K, Kähler CJ, Westerweel J (2005) Main results of the second international piv challenge. Exp Fluids 39:170–191

Stanislas M, Okamoto K, Kähler CJ, Westerweel J, Scarano F (2008) Main results of the third international piv challenge. Exp Fluids 45:27–71

Talamelli A, Segalini A, Örlü R, Schlatter P, Alfredsson PH (2013) Correcting hot-wire spatial resolution effects in third- and fourth- order velocity moments in wall-bounded turbulence. Exp Fluids 54:1496

Tanaka T, Eaton JK (2007) A correction method for measuring turbulence kinetic energy dissipation rate by piv. Exp Fluids 42:893–902

Variano EA, Cowen EA (2008) A random-jet-stirred turbulence tank. J Fluid Mech 604:1–32

Vincent A, Meneguzzi M (1991) The spatial structure and statistical properties of homogeneous turbulence. J Fluid Mech 225:1–20

Westerweel J (1997) Fundamentals of digital particle image velocimetry. Meas Sci Technol 8:1379–1392

Westerweel J, Dabiri D, Gharib M (1997) The effect of a discrete window offset on the accuracy of cross-correlation analysis of digital piv recordings. Exp Fluids 23:20–28

Wyngaard JC (1968) Measurement of small-scale turbulence structure with hot wires. J Phys E Sci Instrum 1:1105